



Article

Lidar Ratio Regional Transfer Method for Extinction Coefficient Accuracy Improvement in Lidar Networks

Yicheng Tong, Sijie Chen , Da Xiao, Kai Zhang, Jing Fang, Chong Liu, Yibing Shen and Dong Liu *

State Key Laboratory of Modern Optical Instrumentation, College of Optical Science and Engineering, International Research Center for Advanced Photonics, Zhejiang University, Hangzhou 310027, China; yichengtong@zju.edu.cn (Y.T.); 11930034@zju.edu.cn (S.C.); 426196@zju.edu.cn (D.X.); 3150104660@zju.edu.cn (K.Z.); 22060074@zju.edu.cn (J.F.); chongliu@zju.edu.cn (C.L.); srr8966@163.com (Y.S.)

* Correspondence: liudongopt@zju.edu.cn; Tel.: +86-1357-578-8748

Abstract: Lidar networks are essential to study the three-dimensional distribution of aerosols on a regional scale. At present, both Mie-scattering lidar (ML) and advanced lidars are being used in lidar networks. The latter can retrieve extinction coefficients without strict assumptions of the lidar ratio, such as Raman lidar (RL) or high-spectral-resolution lidar (HSRL). In order to balance the data quality and instrument costs for the lidar network, the lidar ratio regional transfer method in a lidar network is proposed in this paper. We developed a Lidar Ratio and Aerosol Fraction Non-linear Regression (LR-AFNR) model between the lidar ratio and corresponding absorbing aerosol fraction (this paper studied two types of absorbing aerosols: dust and carbonaceous). The aerosol fraction of the sun photometer retrieval was used as a medium to transfer the lidar ratio of HSRL retrieval to a certain range of MLs. This lidar ratio can be the input parameter for ML retrieval and enables the improvement of the extinction coefficient accuracy. The results show that the LR-APNR model is applicable to atmospheric conditions with high mineral dust or carbonaceous aerosol loading, and the maximum relative error of the ML extinction coefficient can be reduced from 46% (dust) and 64% (carbonaceous aerosol) to 20%.

Keywords: lidar network; lidar ratio; aerosol fraction; sun photometer



Citation: Tong, Y.; Chen, S.; Xiao, D.; Zhang, K.; Fang, J.; Liu, C.; Shen, Y.; Liu, D. Lidar Ratio Regional Transfer Method for Extinction Coefficient Accuracy Improvement in Lidar Networks. *Remote Sens.* **2022**, *14*, 626. <https://doi.org/10.3390/rs14030626>

Academic Editors: Patricia K. Quinn, Maria João Costa, Oleg Dubovik and Jean-Christophe Raut

Received: 7 January 2022

Accepted: 25 January 2022

Published: 28 January 2022

Publisher's Note: MDPI stays neutral with regard to jurisdictional claims in published maps and institutional affiliations.



Copyright: © 2022 by the authors. Licensee MDPI, Basel, Switzerland. This article is an open access article distributed under the terms and conditions of the Creative Commons Attribution (CC BY) license (<https://creativecommons.org/licenses/by/4.0/>).

1. Introduction

Lidar is widely used in atmospheric aerosol detection because of its high temporal, spatial resolution, and continuous monitoring [1]. A lidar network can be used to observe atmospheric aerosols on a regional scale, which is significant in studying the temporal and spatial distributions of regional atmospheric aerosols and the atmospheric pollution control [2,3]. Over the years, several lidar networks have been established, such as the European Aerosol Research Lidar Network (EARLINET) [4], the Asian Dust and Aerosol Lidar Observation Network (AD-Net) [5], and the NASA Micro-Pulse Lidar Network (MPLNET) [6]. EARLINET mainly uses Raman lidar (RL) mainly, while Mie-scattering lidar (ML) and high-spectral-resolution lidar (HSRL) are applied in AD-Net [4,7]. Considering that HSRL and RL can independently retrieve aerosol backscattering and extinction coefficients, we also developed our HSRL system [8]. However, when establishing a lidar network, the HSRL instrument cost is high and difficult to be deployed on an extensive range. If lower-cost ML instruments are used, the aerosol extinction coefficient retrieval accuracy due to a priori assumption is limited [9,10]. Therefore, we considered whether the lidar ratio retrieved by HSRL can be transferred to ML and used as the input parameter of the Klett–Fernald method for retrieval. Then, the extinction coefficient accuracy of multiple MLs in the region will be improved [11,12]. In this way, this mode of single HSRL with multiple MLs can balance the problem of data quality and instrument cost at the same time.

Since HSRL and MLs are not observed at the same location, it is necessary to ensure that the aerosol detected by HSRL is transferred to the atmosphere above ML detection before

directly using the lidar ratio retrieved by HSRL. This process can generally be studied by the Hybrid Single-Particle Lagrangian Integrated Trajectory Model (HYSPLIT) [13]. However, such an ideal situation hardly exists. Automation is essential in actual lidar network observation, and researchers cannot always manually study the processes mentioned above using HYSPLIT. It is not easy to directly transfer the lidar ratio retrieved by HSRL to the ML. Therefore, we considered an indirect transfer of the lidar ratio. The study found a mathematical relationship between the absorbing aerosol lidar ratio and corresponding fraction [14]. By processing the sun photometer data, the fraction of absorbing aerosol will be obtained [15]. In addition, the sun photometer is widely used, and a relatively complete Aerosol Robotic Network (AERONET) has been established by NASA at present [16]. We can place the lidar in the same location with a sun photometer for comparison and verification, which will not add to the cost of sun photometers. Thus, we can use the sun photometer as a medium to indirectly transfer the lidar ratio. It should be noted that the sun photometer retrieves the lidar ratio by applying Mie scattering theory, which is limited by the accuracy of the retrieved size distributions and indices of refraction [17]. Hence, this paper does not use the lidar ratio from the sun photometer retrieval.

In this paper, HSRL and the sun photometer at the same location (centered on this location) are selected to obtain multiple sets of aerosol lidar ratio data and corresponding fraction data. We study two types of absorbing aerosols, which are dust and carbonaceous aerosols (the carbonaceous aerosol here mainly refers to the sum of black carbon (BC) and brown carbon (BrC) [18]). According to the mathematical relationship between the lidar ratio and corresponding aerosol fraction, the Lidar Ratio and Aerosol Fraction Non-linear Regression (LR-AFNR) model is developed. Then, this paper analyzes the reasonable aerosol percentage usage condition and distance usage condition of the model. Under both usage conditions, the aerosol percentage data obtained from another sun photometer (at a certain distance from HSRL) are converted to the lidar ratio by using LR-AFNR. This lidar ratio can be used as an input parameter to the MLs (at the same location as another sun photometer), and the range of improvement in the accuracy of the extinction coefficient of ML after using LR-AFNR is analyzed. This method implements the form of a lidar network consisting of a single HSRL with multiple MLs.

This paper is arranged as follows. In Section 2, the basic principle and implementation processes of the lidar ratio regional transfer method are introduced. The screening criteria for the aerosol (dust and carbonaceous) lidar ratio and corresponding fraction are presented. In Section 3, the LR-AFNR model is developed. The distribution fraction of dust and carbonaceous aerosols obtained from 63 sun photometer sites, as well as the relationship between the lidar ratio relative error and the sun photometer relative distance is studied. In addition, the most suitable distance usage range of the LR-AFNR is determined by analyzing the relative error of the extinction coefficient. In Section 4, we discuss the influence of using the LR-AFNR on the lidar ratio and the influence of different types of aerosols on the LR-AFNR. In Section 5, some concluding remarks are summarized.

2. Materials and Methods

2.1. Lidar Ratio Regional Transfer Method

The schematic diagram of the lidar ratio regional transfer method and the spatial distribution of the lidar network are as follows (Figure 1): the sun photometer (No. 0) with the HSRL at the same location is chosen as the center, and the LR-AFNR model is established by the mathematical relationship between the lidar ratio obtained by the HSRL and the corresponding aerosol fraction obtained by the sun photometer. The aerosol fraction data obtained from the sun photometers (No. 1~n) are converted into lidar ratio data using the LR-AFNR under certain distance and aerosol fraction usage conditions. The lidar ratio can be used as input parameters for ML (No. 1~n) at the same location, enabling the regional transfer of HSRL to the ML lidar ratio. Figure 1b represents the lidar network mode of HSRL combined with MLs mentioned in this paper. We show the spatial distribution of different instruments in the lidar network. The distance between the HSRL

and MLs needs to be kept within a certain range to meet the basic error requirements, and the specific error analysis will be discussed below.

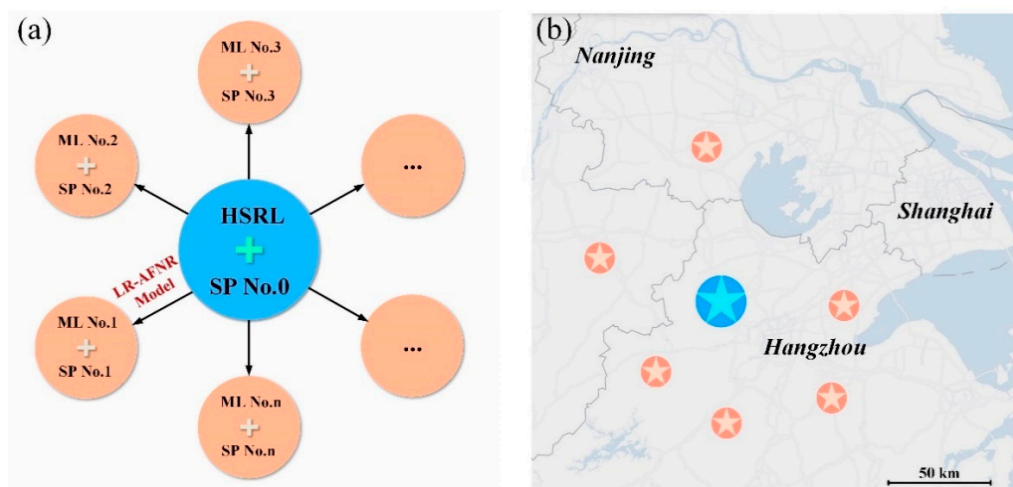


Figure 1. The schematic diagram of the lidar ratio regional transfer method and the spatial distribution of the lidar network. (a) The schematic diagram of the lidar ratio regional transfer method. The blue circle in the figure represents the combination of HSRL and the sun photometer (SP) at the same position, and the orange circle represents the combination of ML and the sun photometer (SP) at the same position. The direction of the arrow represents the lidar ratio transfer from HSRL to different MLs using the LR-AFNR. No. 0– n represents the instrument number ($n \geq 1$); (b) Schematic of the spatial distribution of the lidar network of HSRL combined with MLs. The blue and orange pentagons correspond to the two combinations of the lidar and sun photometer mentioned in figure (a).

The main process of the lidar ratio regional transfer method includes six steps of data acquisition, data retrieval, data screening, developing the LR-AFNR model, determining the conditions for using the LR-AFNR, and completing the lidar ratio regional transfer (Figure 2). The specific steps are as follows: First, obtain the relevant data from the HSRL and sun photometer (HSRL and AERONET sites need to be selected in the same location). The data of different lidar ratios and the corresponding aerosol fractions are obtained by retrieving the above two data sources. Then, we proposed the data screening criteria for different lidar ratios and corresponding aerosol fractions and screened the relevant data. The lidar ratio with corresponding aerosol fraction data was selected for the same location and the same hour of observation, and the LR-AFNR model was developed. After that, the conditions of use of LR-AFNR (aerosol fraction and distance conditions) need to be determined. Finally, the aerosol fraction was converted to the lidar ratio based on the conditions of use of LR-AFNR. At the same time, it was used as an input parameter for ML using the Klett–Fernald retrieval method [11].

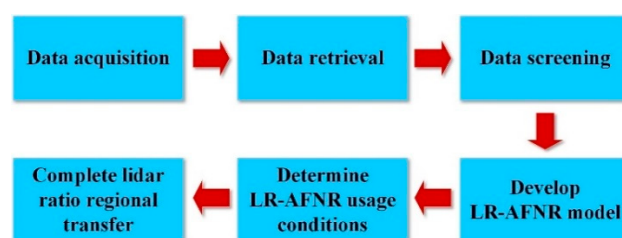


Figure 2. Flowchart of the lidar ratio regional transfer method. The flowchart consists of six steps: data acquisition, data retrieval, data screening, developing the LR-AFNR model, determining the conditions for using the LR-AFNR, and completing the lidar ratio regional transfer.

2.2. Screening of Different Lidar Ratio Data

Taking advantage of the broad spectrum of Cabannes–Brillouin scattering from atmospheric molecules, the HSRL technique employs a narrow spectral filter to reject the aerosol Mie-scattering component in the lidar return signals. Therefore, the HSRL can directly obtain the aerosol extinction coefficient and backscatter coefficient [19,20]. The lidar ratio can be calculated from these two parameters. Considering a mathematical relationship between the fraction of dust or carbonaceous aerosols with the lidar ratio [14], the lidar ratio obtained by HSRL is first screened. This paper selects the data of the University of Wisconsin HSRL (UW-HSRL) [21], and the three sites selected are shown in Table 1. The first site is named northern Great Plains (SGP) and is located on the northern plains of Oklahoma. This system (BagoHSRL) has ceased observation (belongs to the archived site). We downloaded observations data for this system from January 2015–October 2017. The second site is named KORUS and is located at Yonsei University in Seoul, Korea. This system (AHSRL) has ceased observation (belongs to the archived site). We downloaded observations data from this system from January 2016–December 2018. The third site is named Madison, WI, located at the University of Wisconsin–Madison in Wisconsin. This system (BagoHSRL) maintains routine observations (belongs to the active site). We downloaded the observation data of the system from November 2012–June 2019. The wavelength and altitude ranges of the data are 532 nm and 0–10 km, respectively. In addition, the spatial and temporal resolutions of the data are 7.5 m and 10 min, and the download formats and file modes of the data are NetCDF4 and day, respectively. Details can be found at <http://hsrl.ssec.wisc.edu> (last accessed on 26 April 2021).

In this paper, the parameter retrieval using the UW-HSRL included the aerosol depolarization ratio δ_a , aerosol backscatter coefficient β_a , aerosol extinction coefficient α_a , and lidar ratio $S_a = \alpha_a / \beta_a$. In order to make a more reasonable comparison with the sun photometer data, this paper needs to make an assumption about column properties: the aerosol is well-mixed in the entire boundary layer [22]. Considering the existence of a near-surface layer of more than 4 km [23–25], the near-surface layer of this paper is selected to be 4 km, i.e., the altitude range of HSRL data selection is 0.5–4 km (removal of the part affected by the overlap factor below 0.5 km).

Table 1. The information of UW-HSRL sites, which includes the site name, system name, longitude, latitude, and data selection period.

| Site Name | System Name | Latitude (°) | Longitude (°) | Selection Period |
|-----------|-------------|--------------|---------------|----------------------------|
| SGP | BagoHSRL | 36.62 N | 97.49 W | January 2015–October 2017 |
| KORUS | AHSRL | 37.56 N | 126.95 E | January 2016–December 2018 |
| Madison | BagoHSRL | 43.01 N | 89.41 W | November 2012–June 2019 |

Based on [26], the authors found pure dust $\delta_a = 0.3$ and pure carbonaceous aerosol $\delta_a = 0.05$. When dust and carbonaceous aerosols are uniformly mixed, as well as the dust fraction of total backscatter (called the dust absorbing mixing ratio) in the range of 50–100%, dust is considered to be the primary absorbing aerosol with δ_a values ranging from 0.15–0.3. It should be noted that the dust (carbonaceous aerosol) absorbing mixing ratio refers to the fraction of dust (carbonaceous aerosol) to the total sum of dust and carbonaceous aerosols. On the contrary, the carbonaceous aerosol is considered the main one with δ_a values ranging from 0.05 to 0.15, while the carbonaceous aerosol absorbing mixing ratio range is 50–100%. In order to distinguish between dust and carbonaceous aerosols, we also need to use the lidar ratio. According to relevant historical documents, the polluted dust lidar ratio range is 30–60 Sr, and the polluted carbonaceous aerosol lidar ratio range is 40–100 Sr [27–33]. In addition, to eliminate the influence of cloud and low signal-to-noise data, the scattering ratio $R = (\beta_m + \beta_a) / \beta_m$ is set in the range of 1.2–10 [8,34]. β_m is the backscatter coefficient of atmospheric molecules, which can be obtained through the 1976 U.S. Standard Atmosphere Model. Considering that aerosols may still occur above 4 km,

this paper adopts the method of [8] to set a threshold value of the scattering ratio R to screen data with aerosols. We established the theoretical scattering ratio threshold T_t and the practical scattering ratio threshold T_p . The expressions are

$$T_t = 1, \quad (1)$$

$$T_p = \frac{\sigma\beta_a + \beta_m}{\beta_m}. \quad (2)$$

where $\sigma\beta_a$ represents the uncertainty of aerosol backscatter, and the specific calculation method can be found in Equations (3)–(5), (14) and (17)–(21) mentioned in the paper of [8]. When the altitude is greater than 4 km and $R > T_p$, we consider the presence of aerosols and discard the lidar ratio profile data. Therefore, the lidar ratio screening criteria (Table 2) are proposed for dust and carbonaceous aerosols. The lidar ratio data outside the reasonable range of the criteria are set to the NaN value. It should be noted that the dust-dominated and carbonaceous aerosol-dominated screening criteria are only different in the aerosol depolarization ratio and lidar ratio.

Table 2. The screening criteria for the lidar ratio data when dust or carbonaceous aerosols are the dominant type.

| | Dust-Dominated Data | Carbonaceous Aerosol-Dominated Data |
|-------------------------------------|---------------------|-------------------------------------|
| Height (km) | 0.5–4 | 0.5–4 |
| Aerosol depolarization ratio (unit) | 0.15–0.3 | 0.05–0.15 |
| Scattering ratio (unit) | 1.2–10 | 1.2–10 |
| Lidar ratio (Sr) | 30–60 | 40–100 |
| Absorbing mixing ratio (%) | 50–100 (dust) | 50–100 (carbonaceous aerosol) |
| Scattering ratio above 4 km (unit) | $T_t < R < T_p$ | $T_t < R < T_p$ |

This paper only takes the observation results of the KORUS site on 21 April 2017 as an example (Figure 3) to show the results of the lidar ratio screening.

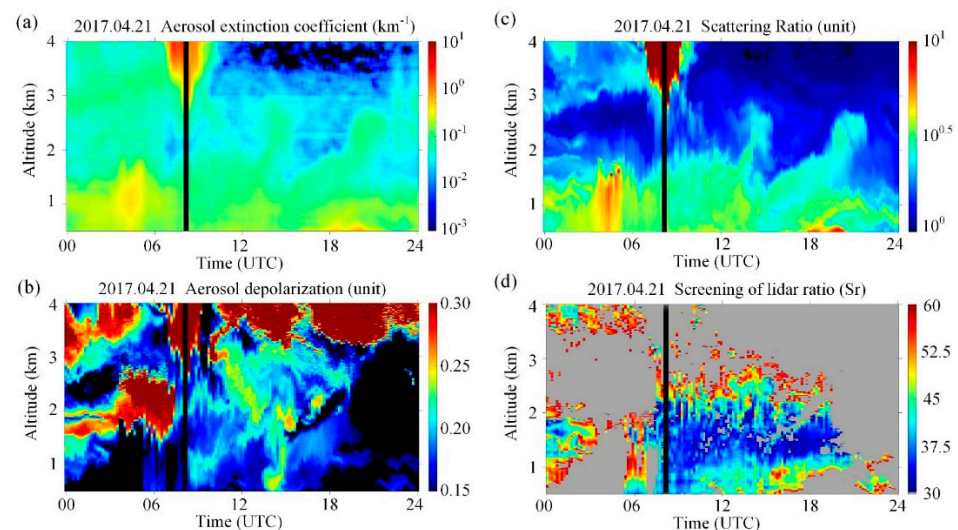


Figure 3. The screening results of dust-dominated observations with the lidar ratio at the KORUS site based on HSRL on 21 April 2017. (a) Aerosol extinction coefficient; (b) Scattering ratio; (c) Aerosol depolarization ratio; (d) Selection of dust-dominated lidar ratio result by screening criteria (grey represents the screened part).

The lidar ratio data retrieved from the three HSRL sites was screened with dust-dominated data and carbonaceous aerosol-dominated data through screening criteria. The

data mentioned above were averaged at a spatial resolution of 0.5–4 km and a time period of one hour.

2.3. Retrieval Method of Aerosol Fraction and Data Screening

AERONET is a globally distributed network of automated sun and sky radiometers, which measure the aerosol optical depth (AOD) and absorption aerosol optical depth (AAOD) at four wavelengths (440, 675, 870, and 1020 nm), as well as other properties [35]. This paper uses the Level 1.5 and Version 3 data from AERONET. Details can be found at <https://aeronet.gsfc.nasa.gov> (last accessed on 23 March 2021) [36]. Since this paper needs to use single-scattering albedo (SSA) data with AOD < 0.4, and level 2.0 data only have SSA data when AOD > 0.4, the data of level 1.5 were used in this paper [35]. Three AERONET sites were selected that overlap with the HSRL sites (Table 3) in the previous section.

Table 3. The information of AERONET sites, which includes the site name, location, longitude, latitude, and data selection period.

| Site Name | Location | Latitude (°) | Longitude (°) | Selection Period |
|---------------------|--------------------------|--------------|---------------|----------------------------|
| Cart | Oklahoma, United States | 36.61 N | 97.49 W | January 2015–December 2018 |
| Yonsei University | Seoul, South Korea | 37.56 N | 126.94 E | January 2016–December 2018 |
| U of Wisconsin SSEC | Wisconsin, United States | 43.01 N | 89.41 W | November 2012–June 2019 |

Based on [15], the authors proposed a method combining the absorption Angstrom Exponent (AAE) in visible and near-UV spectra to separate the total AAOD observed by the sun photometer into BC, BrC, and dust, where the AAE value of each absorbing component is assumed known and constant; the expression is

$$AAOD(\lambda_i) = AAOD_{ref,BC} \left(\frac{\lambda_i}{\lambda_{ref}} \right)^{-AAE_{BC,i}} + AAOD_{ref,BrC} \left(\frac{\lambda_i}{\lambda_{ref}} \right)^{-AAE_{BrC,i}} + AAOD_{ref,dust} \left(\frac{\lambda_i}{\lambda_{ref}} \right)^{-AAE_{dust,i}} \quad (3)$$

where there are two inherent assumptions in Equation (3): (1) The AAE value of each absorbing component is an intrinsic property that does not depend on the mixing state and (2) the measured AAOD value represents a well-mixed sample of these species. Based on the two assumptions mentioned above, the Equation (3) of AAOD for different absorbing components can be developed at three different wavelengths λ_i (440, 675, and 870 nm). The Equation (3) can provide three equations with three unknowns. AAE values for $\lambda_1 = 440$ nm and $\lambda_2 = 675$ nm are denoted as AAE1, and AAE values for $\lambda_1 = 675$ nm and $\lambda_2 = 870$ nm are denoted as AAE2. Based on [15], the authors showed that AAE1 values of BC, BrC, and dust are calculated to be 0.55 ± 0.24 , 4.55 ± 2.01 , and 2.20 ± 0.50 , respectively, and AAE2 values of BC and dust are calculated to be 0.85 ± 0.40 and 1.15 ± 0.50 , respectively. It should be noted that the AAE2 of BrC is not defined because BrC has minimal absorption in near-infrared spectra, and it is assumed that BrC does not absorb at 870 nm. Since the wavelength of UW-HSRL data used in this paper is 532 nm, the data of this wavelength are not available in AERONET. Therefore, it is necessary to convert the extinction Angstrom Exponent (EAE), AAE, AOD, and AAOD between different wavelengths to calculate the correlation result for $\lambda_{ref} = 532$ nm. The conversion equation is as follows [15,22]:

$$AOD(\lambda_1) = -AOD(\lambda_2) \cdot \left(\frac{\lambda_1}{\lambda_2} \right)^{-EAE} \quad (4)$$

$$AAOD(\lambda_1) = -AAOD(\lambda_2) \cdot \left(\frac{\lambda_1}{\lambda_2} \right)^{-AAE} \quad (5)$$

where λ_1 and λ_2 represent different reference wavelengths ($\lambda_1 = 440$ nm, $\lambda_2 = 532$ nm). Equations (4) and (5) can be used to convert $AOD(440)$ and $AAOD(440)$ into $AOD(532)$

and $AAOD(532)$, respectively. The corresponding EAE and AAE values can be obtained directly from the AERONET Version 3 data product. In addition, the relationship between AOD , SSA , and $AAOD$ is also satisfied

$$AOD = AAOD / (1 - SSA). \quad (6)$$

Based on [15], SSA values of BC , BrC , and dust at 550 nm were found to be 0.225 ± 0.075 , 0.9 ± 0.05 , and 0.925 ± 0.025 , respectively. For both AAE and SSA above, we chose the average value to be used in the Equation (6) for calculation. One-hour average AOD values of the three absorbing aerosols of BC , BrC , and dust in the corresponding observation period were calculated by the Equation (6). Then, the values were normalized to obtain the percentage of BC , BrC , dust, and other aerosols at each of the three sites at the corresponding observation period (take the sum of BC and BrC as carbonaceous aerosols). Since the South Korean region is greatly affected by the dust transfer from the Gobi in spring [37], the average monthly fraction of dust in March and April each year at the Yonsei University site was selected for the study. In the United States, a large number of carbonaceous aerosols are produced in the summer and autumn due to agricultural waste and wildfire burning [38]. Thus, the monthly average carbonaceous aerosol fraction from July to October at the Cart site was selected for the study (Figure 4).

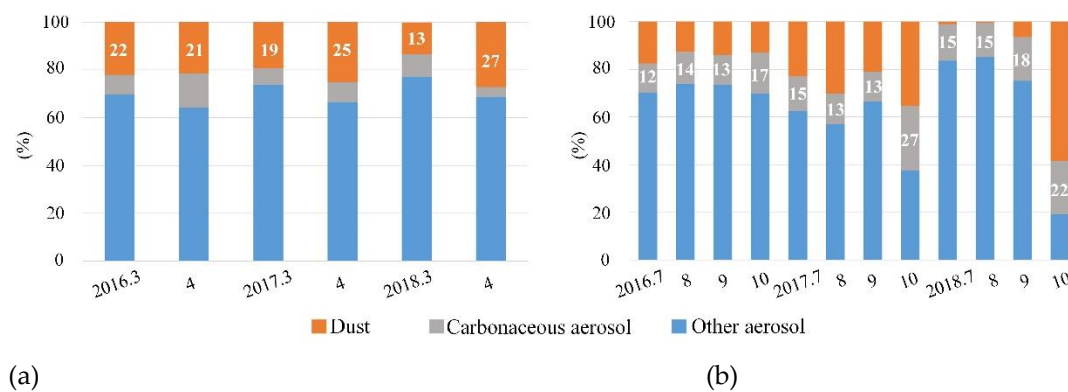


Figure 4. Statistics of the monthly average fraction of relevant absorbing aerosols at the three sites in the selected period. (a) The monthly average fraction distribution of dust, carbonaceous aerosol, and other aerosols at the Yonsei University site in March and April each year from 2016 to 2018; (b) The monthly average fraction distribution of dust, carbonaceous aerosol, and other aerosols at the Cart site from July to October of each year from 2016 to 2018.

The average dust fraction at the Yonsei University site in March and April of each year during the period selected in this paper was calculated as 21.1%. The average carbonaceous aerosol fraction at the Cart site from July to October was calculated as 16.1%. For convenience, the data of dust and carbonaceous aerosol fractions exceeding 20% and 15% were selected for the following study.

3. Results

3.1. Development of a Non-Linear Regression Model

A non-linear regression model of two lidar ratio and corresponding aerosol fractions was developed (Figure 5). It should be noted that the fraction of dust (carbonaceous aerosol) represented by the horizontal coordinate in Figure 5 refers to the proportion of dust (carbonaceous aerosol) in the total aerosols. In addition to dust and carbonaceous aerosols, total aerosols also include other absorbing and non-absorbing aerosols. The dust (carbonaceous aerosols) absorbing mixing ratio refers to the fraction of dust (carbonaceous aerosols) to the total sum of dust and carbonaceous aerosols. Referring to [14], the non-

linear regression model is fitted using only simple quadratic polynomial functions (i.e., $y = ax^2 + bx + c$).

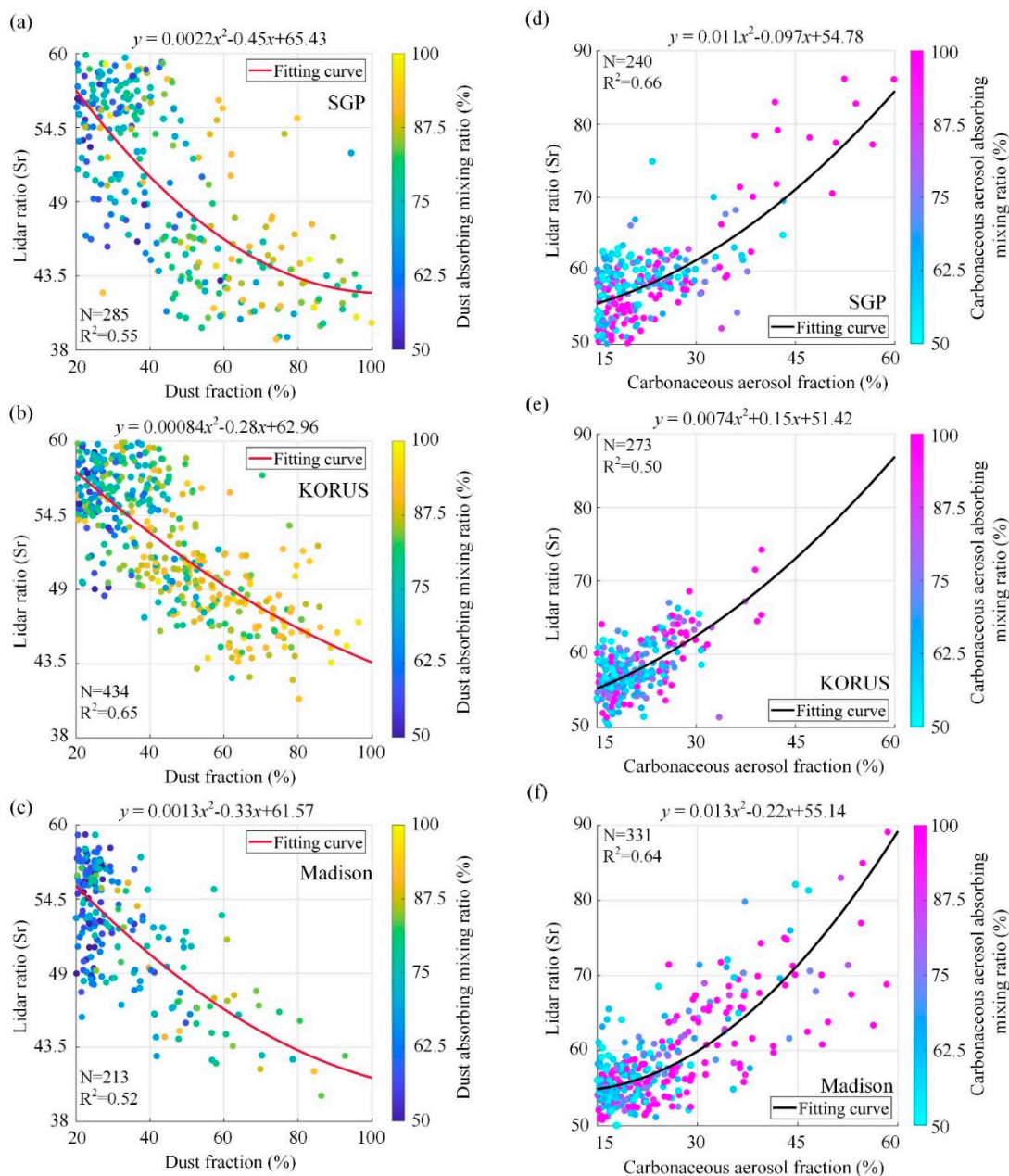


Figure 5. Scatter plot of the absorbing aerosol lidar ratio retrieved by HSRL and fraction retrieval by the sun photometer. N and R² represent the number of fitting points and coefficient of determination, respectively. (a–c) represent the fitting relationship of the lidar ratio and dust fraction at the SGP, KORUS, and Madison sites, respectively. The solid red line represents the fitting results, and the color bar represents the dust absorbing mixing ratio; (d–f) represent the fitting relationship of the lidar ratio and carbonaceous aerosol fraction at the SGP, KORUS, and Madison site, respectively. The solid black line represents the fitting results, and the color bar represents the carbonaceous aerosol absorbing mixing ratio. The top of the subplot represents the equation of the fitted curve.

Based on Figure 5, the R² of fitting curves between the two absorbing lidar ratios retrieved by HSRL and the corresponding percentage retrieved by the sun photometer were both greater than 0.5, which can be considered to be highly correlated [39]. The fitting lidar ratio in Figure 5a–c decreased gradually with an increase in the dust fraction. Because

the three sites selected in this paper are all located inland, with the lack of a mixture of aerosols with a low lidar ratio similar to sea salt aerosols, it can be considered that the dust studied in this paper is mainly polluted dust. With the increase in the dust fraction, the results approach the lidar ratio of pure dust, which is generally 35–50 Sr [30]. Further, the trends of the dust-dominated lidar ratio fitting curves are similar to the results of [14]. The fitting lidar ratio in Figure 5d–f increases gradually with the increase in the carbonaceous aerosol fraction. We consider that this part of the carbonaceous aerosol may contain a mixture of smoke with relatively high lidar ratio [31]. We used the average of the fitting curves in Figures 5a–c and 5d–f as the LR-AFNR model for dust and carbonaceous aerosols, respectively.

3.2. Usage Conditions of the Model

3.2.1. Screening of AERONET Sites

After developing the LR-AFNR model, it is necessary to clarify the usage conditions of this model. This paper uses AERONET data from different sites to carry out the study on the usage conditions considering that dust in Asia and carbonaceous aerosols in Europe and the United States are more typical [7]. The AERONET sites in the regions mentioned above are relatively concentrated, and there are numerous downloadable data. Thus, this paper selected the data of 63 sites in six regions to carry out the study. The distribution of sites can be found in Figure A1 of Appendix A. In addition, the site name, location, and data selection period information can be found in Table A1 of Appendix A (the altitude of all selected sites was less than 0.5 km).

The six AERONET sites of the ① MD Science Center, ② Mainz, ③ Carpentras, ④ Beijing, ⑤ Taihu, and ⑥ Yonsei University were taken in the six regions mentioned above as the center, and the data of a total of 63 sites were selected within 500 km around the central sites to study the usage conditions of the LR-AFNR [36].

3.2.2. Distribution of the Aerosol Fraction and Distance Usage Conditions

According to Equations (3)–(6), the dust and the carbonaceous aerosol fraction of 63 sites with a time resolution of one hour were calculated. We compared the probability distribution of dust and carbonaceous aerosol fractions in the six regions in Figure 6. The fraction probability exceeded 0.4 concentrated in a range of 20–40% for dust. For carbonaceous aerosol (the horizontal coordinate (10–20% of the scale) actually included only 15–20% of the fraction), the fraction probability exceeded 0.4 concentrated in a range of 15–20%. According to the calculation results, it was found that the probability of the carbonaceous aerosol fraction exceeding 60% in all six regions was less than 0.02. Thus, the condition that the carbonaceous aerosol fraction exceeded 60% was not considered. This paper defines the dust fraction in the range of 20–40% as light dust and that in the range of 40–100% as heavy dust. At the same time, the carbonaceous aerosol fraction in the range of 15–20% or 20–60% is considered light carbonaceous aerosol or heavy carbonaceous aerosol, respectively.

Based on the four types of absorbing aerosol fractions mentioned above, the distribution of the lidar ratio relative error with distance was studied using data from different sun photometer sites. The fractions of dust and carbonaceous aerosols obtained by any two sun photometer sites (assumed names A and B) were used as input parameters into the LR-AFNR and converted into the lidar ratio. Then, the average lidar ratio for the same hour at sites A and B was calculated within the period selected in Table A1. The lidar ratio obtained in the atmosphere over site A was taken as the actual value of site A, and the lidar ratio obtained at site B was taken as the reference value of site A. The relative distance between sites of A and B, as well as the average of the lidar ratio relative error for a temporal resolution of one hour within the selected period was calculated (here, the relative error was taken as the absolute value). It should be noted that the relative distance between the selected two sites should be less than 500 km, and the total number of data

points used to calculate the average lidar ratio relative error between the two sites should be greater than 50.

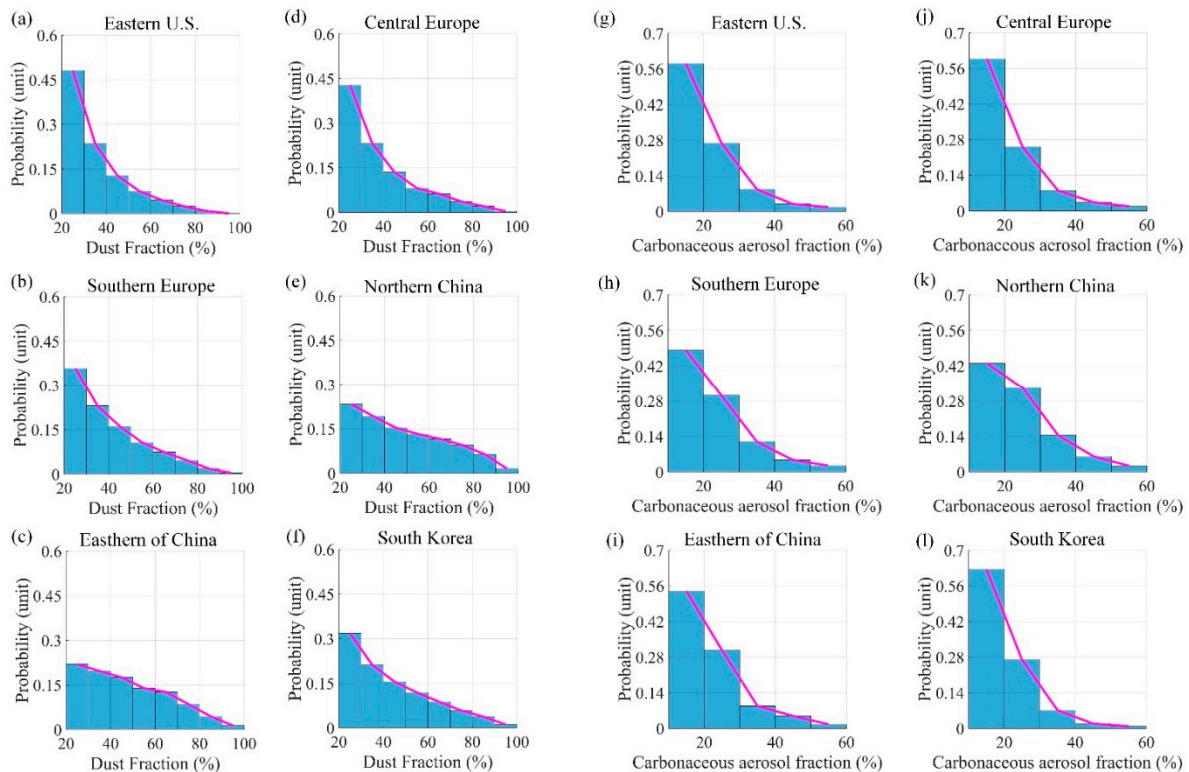


Figure 6. The probability distribution of dust and carbonaceous aerosol fractions in six regions (eastern U.S., central Europe, southern Europe, northern China, eastern China, and South Korea). (a–f) represent the probability distribution of the dust fraction in the six respective regions; (g–l) represent the probability distribution of the carbonaceous aerosol fraction in the six respective regions, where the horizontal coordinate (10–20% of the scale) actually includes only 15–20% of the fraction.

The data from any two sun photometer sites in the six regions mentioned above were compared to obtain a series of the relationship of the relative distance and average relative error of the lidar ratio for the four types of light/heavy dust, light/heavy carbonaceous aerosols (Figure 7). Based on the results shown in the scatter of Figure 7, we used the inverse tangent function (i.e., $y = a \cdot \arctan(bx)$) for the fit.

Through the screening conditions mentioned above, the final effective data points under the four different aerosol absorbing conditions are 100, 88, 70, and 98, respectively. Figure 7 illustrates that when the relative distance between AERONET sites increases, the relative error of the lidar ratio also becomes larger but finally tends to a stable value. Moreover, under the conditions of heavy dust and heavy carbonaceous aerosols, the final tendency of the lidar ratio relative error in the six regions is much larger than that under the conditions of light dust and light carbonaceous aerosols. The main reason is that the maximum absorbing aerosol fraction does not exceed 100%, limiting the relative error of the lidar ratio. Since the lidar ratio directly affects the retrieval accuracy of α_a using the Klett–Fernald method, the effect of the LR-AFNR on the relative error of α_a is used to study the range of usage distance. The results mentioned above will be discussed and analyzed in more detail in the next section (the selection of points A, B in Figure 7 are introduced in the next section).

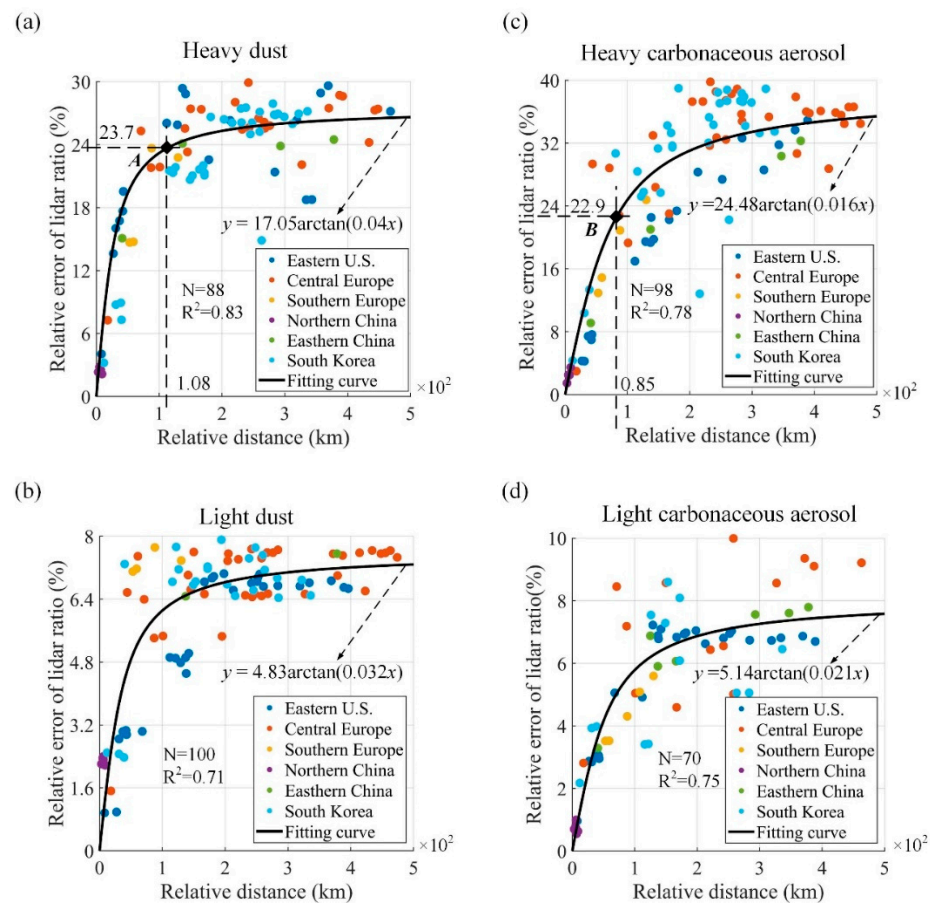


Figure 7. The scatter-fitting relationship between the relative distance and the relative error of the lidar ratio under different aerosol absorbing conditions. The six different scatter colors represent the lidar ratio average relative error between any two sites in the six regions of the eastern US, northern Europe, northern Europe, northern China, eastern China, and South Korea. The solid black line represents the fitting curve, and N and R^2 represent the total number of fitting points and the coefficient of determination for the six regions, respectively. (a) Under the condition of heavy dust, point A represents the intersection of the lidar ratio relative error of 23.7% and the relative distance of 108 km; (b) Under the condition of light dust; (c) Under the condition of heavy carbonaceous aerosols, point B represents the intersection of the lidar ratio relative error of 22.9% and the relative distance of 85 km; (d) Under the condition of light carbonaceous aerosols. The dashed line in the subplot points to the equation of the fitted curve.

3.3. Error Analysis

In the previous section, we analyzed the relationship between the lidar ratio relative error and the different relative distances of the instruments using the LR-AFNR under four different aerosol conditions (light/heavy dust, light/heavy carbonaceous aerosols). However, we did not obtain the most suitable range for using the LR-AFNR model. According to [40], the use of α_a as a parameter for the retrieval of aerosol microphysical properties is meaningful only when its uncertainty is less than 20%. We therefore limited the maximum allowed relative uncertainty of the extinction coefficient to 20%. Next, the lidar ratio relative error was derived from the extinction coefficient relative error. Then, the corresponding relative distance was determined from the lidar ratio relative error. Based on [41], we performed a correlation error study using the lidar simulation signal. HSRL system parameters as well as basic parameters for lidar signal simulation were adopted from [42]. Specific information can be found in Table A2 of Appendix A. The aerosol loading was set to the bottom exponential aerosol type [43–45], and the boundary layer height was set at 3 km. In addition, the average values of AOD were calculated for 63 sites with a dust fraction

greater than 20% and carbonaceous aerosol fraction greater than 15%, which were 0.36 and 0.31, respectively. Therefore, the simulation set $AOD = 0.36$ for the dust-dominated condition and $AOD = 0.31$ for the carbonaceous aerosol-dominated condition. The actual lidar ratio was calculated by LR-AFNR, ranging from 42.4–56.8 Sr and 54.3–87.9 Sr under dust and carbonaceous aerosol conditions, respectively. Furthermore, the reference lidar ratio was the initial lidar ratio when the Klett–Fernald method was used, set in the range of 30–60 Sr and 40–100 Sr for dust and carbonaceous aerosol conditions, respectively. The values of β_m , α_m (atmospheric molecular extinction coefficient) were calculated by the 1976 U.S. Standard Atmosphere Model. The background aerosol scattering ratio was set to 1.02 [46]. In this study, Poisson noise was added as the main error source [47,48]. Through the above-mentioned basic parameter setting, a lidar simulation signal was simulated.

It should be noted that the lidar ratio was set to a constant, and each simulated signal was averaged 500 times. The retrieval used the Klett–Fernald method [11] and started from the boundary layer at 3 km, and the initial reference β_a used the actual value of the simulation. The results (Figure 8) were retrieved using 50 simulated signal profiles.

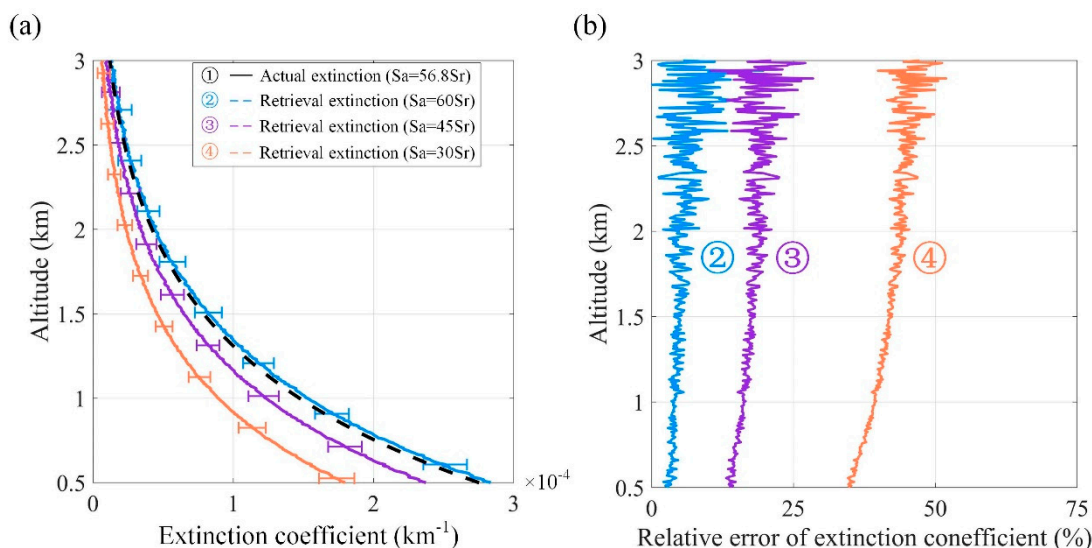


Figure 8. Take dust as an example, the Klett–Fernald method was used to retrieve the α_a , as well as the relative error distribution of α_a . (a) The results of α_a retrieval using 50 simulated signal profiles in the 3 km boundary layer. The dotted black line (①), the solid blue line (②), the solid purple line (③), and the solid orange line (④) represent the simulated actual α_a (the lidar ratio was 56.8 Sr) and the average of α_a retrieval after substituting three reference lidar ratios (lidar ratios of 60, 45, and 30 Sr). The three error bars represent the standard deviation of α_a retrieval using the three reference lidar ratios (b) Relative error profile of α_a retrieval using three reference lidar ratios.

Based on Figure 8, the larger the relative error of the lidar ratio, the larger the relative error of the α_a retrieval. The simulated signal had a relative error greater than 40% for the extinction coefficient due to the lidar ratio relative error.

The aerosol actual lidar ratio and the reference lidar ratio were taken as the horizontal and vertical coordinates, respectively, and each corresponding coordinate calculated a relative error profile of α_a , similar to Figure 8b. The average value of this profile was calculated (as the absolute value). At the same time, the relative error of the lidar ratio was calculated (as the absolute value). The above-mentioned two average values were used as the third coordinate to obtain the results (Figure 9).

Combined with Figure 7, the relative error of α_a varied with the distance between the two AERONET sites. Since the horizontal and vertical coordinates of the relative error of α_a and the lidar ratio had the same value, the relative error of the dust and carbonaceous aerosol lidar ratio was calculated according to the limit of α_a , i.e., a relative error of 20%.

As shown by the black dotted lines in Figure 9b,d, the relative error of the two aerosol lidar ratios was limited to 23.7% and 22.9% (the average of the values of the upper and lower black solid lines). Based on a comparison with the results of Figure 7, the above-mentioned relative error in Figure 7a,c corresponded to 108 km (point A) and 85 km (point B), respectively. In other words, after using LR-AFNR to obtain the lidar ratio, the range of the relative error of dust α_a and carbonaceous aerosol α_a was 4–20% when the distance between ML and HSRL was within 108 km and 85 km (4% was the minimum relative error of the signal simulation). According to the calculated results, the range of the dust α_a relative error in Figure 9a was 4–43% (including the grey part), and the range of the carbonaceous aerosol α_a relative error in Figure 9c was 4–64% (including the grey part), which indicated that after using the LR-AFNR, HSRL had a significant improvement in the accuracy of ML retrieving α_a for the same range, and the maximum relative error of dust and carbonaceous α_a decreased from 43% and 64% to 20%.

Nevertheless, the relative error of the lidar ratio in Figure 7b,d was smaller, and the relative error of α_a did not exceed 20%. The relative error of α_a was not caused primarily by the relative error of the aerosol fraction under the condition of light dust and light carbonaceous aerosols.

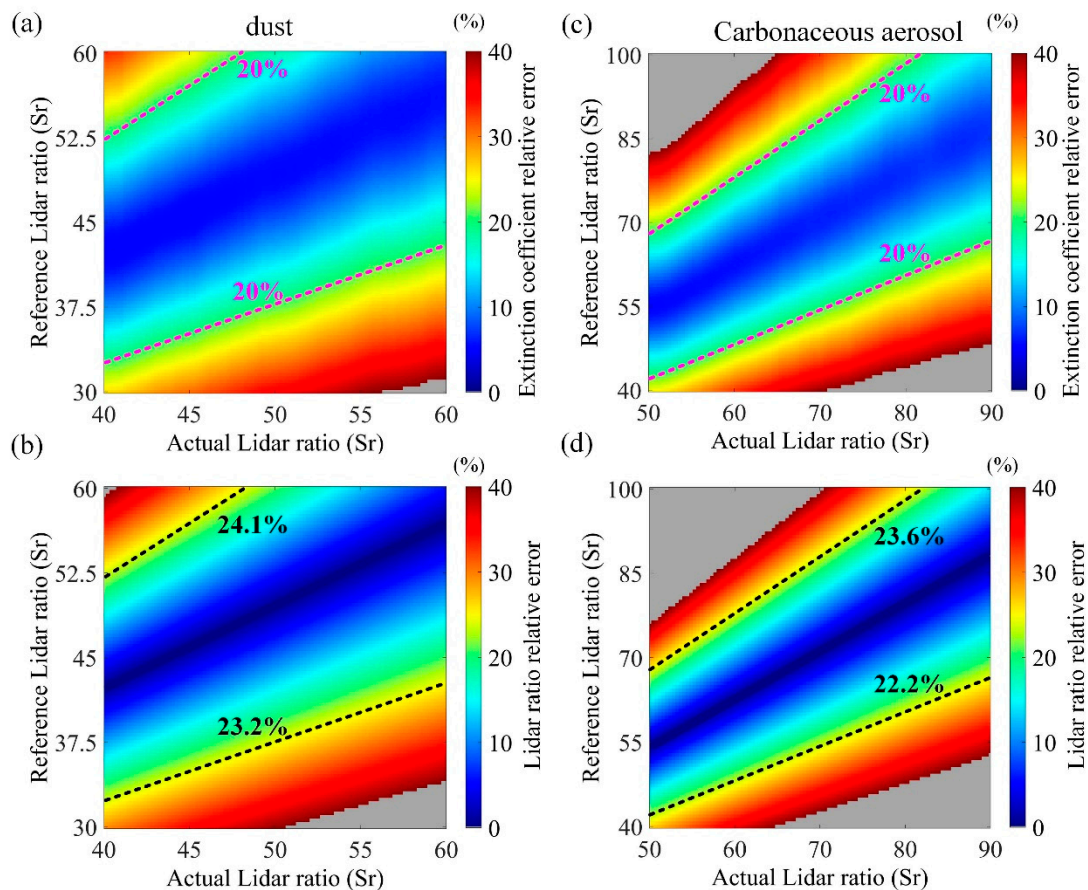


Figure 9. The relationship between the relative error of α_a and the lidar ratio, as well as the actual lidar ratio and the reference lidar ratio. (a,b) represent the relative error of α_a and the lidar ratio under the dust condition; (c,d) represent the relative error of α_a and the lidar ratio under the carbonaceous aerosol condition. The pink dotted line represents the position where the relative error of α_a was 20%, and the black dotted line represents the relative error of the lidar ratio at the same position (same horizontal and vertical coordinates) as the pink dotted line in the figure. The grey area represents the part that exceeded the upper limit of the color bar.

4. Discussion

4.1. The Influence of the LR-AFNR Model on the Lidar Ratio

This section will discuss the influence of different aerosol fractions on the lidar ratio after using LR-AFNR. Here, only dust is taken as an example. Assuming that the actual value of the dust fraction of site A is $X\%$, the reference value of site B should be $20\text{--}100\%$, and the absolute error of the dust fraction can be in the range of $(20 - X\%)$ – $(100 - X\%)$. The above-mentioned actual value of site A and the reference value of site B were input parameters into the LR-AFNR, and the relative error of the corresponding lidar ratio was calculated. According to this calculation method, the actual value of the dust fraction was the horizontal coordinate, and the absolute error range of the dust fraction was the vertical coordinate. The relative error of the lidar ratio was the third coordinate. After changing the value of X from $20\text{--}100\%$, we obtained the results shown in Figure 10a.

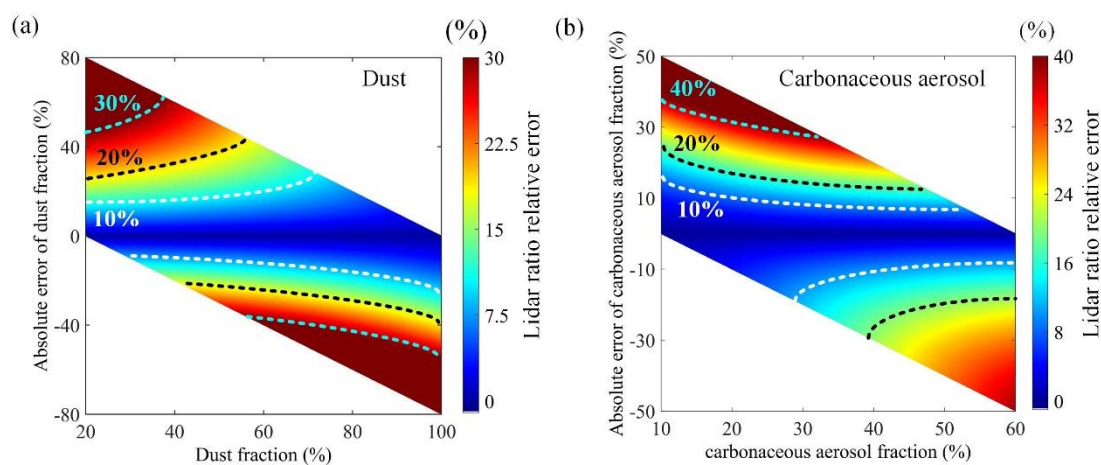


Figure 10. The relationship between the two absorbing aerosol fractions and the lidar ratio relative error. The horizontal and vertical coordinates represent the actual value of the two absorbing aerosol fractions and the absolute error of the reference value, respectively. The color bar represents the relative error of the lidar ratio calculated after the two absorbing aerosol fractions were input into the LR-AFNR. The white part in the figure represents no data. (a) Under the condition of dust, the sky blue, black, and white dotted lines represent the positions where the relative error of the lidar ratio was 30%, 20%, and 10%, respectively; (b) Under the condition of carbonaceous aerosol, the sky blue, black and white dotted lines represent the positions where the relative error of the lidar ratio was 40%, 20%, and 10%, respectively.

In Figure 10a, under the condition of heavy dust, the range of the dust fraction was $40\text{--}100\%$. When two AERONET sites were relatively close to each other, the difference between the actual value of the dust fraction and the reference value was small, and the relative error of the lidar ratio value fell in the area within 20% of the dotted line of Figure 10a. However, due to the upper limit of the dust fraction, the relative error of the lidar ratio did not continue to increase with the relative distance and eventually stabilized. Thus, the value fell in the dotted line area between $20\text{--}30\%$ in Figure 10a. Under the condition of light dust, the range of the dust fraction was $20\text{--}40\%$ because the fraction itself was relatively small. Therefore, the relative error value of the lidar ratio basically fell within the dark blue area in Figure 10a, and the relative error of the lidar ratio did not continue increasing with the relative distance and eventually stabilized. The above-mentioned analysis also explains the scatter plot distribution of the lidar ratio relative error and the relative distance in Figure 7.

4.2. The Influence of Different Types of Aerosols on the LR-AFNR Model

When we used Equations (3)–(6) to calculate the BC, BrC, and dust fraction, the AAE and SSA values used were the average of the reference values. However, in fact, the

AAE and SSA values of different types of carbonaceous aerosols are also different [49,50]. According to [51], we found that the AAE and SSA of fresh smoke in carbonaceous aerosol was lower than the corresponding value of aged smoke (where fresh refers to smoke formed within 5 min and aged refers to smoke from one hour to several days old). To facilitate comparing the influence of different aerosol types (i.e., different AAE and SSA values) on the LR-AFNR, we assumed that the lower AAE and SSA values were for carbonaceous aerosols dominated by fresh smoke. On the contrary, they are carbonaceous aerosols dominated by aged smoke. We set 0.9 and 1.1 times the average value of AAE in Section 2.3 (both within the range of reference values given by [15]) under the condition of fresh smoke and aged smoke, respectively, and the lower and upper limits of the SSA reference values were set under the condition of fresh smoke and aged smoke, respectively (Table 4). In addition, the AAE and SSA values of dust remained unchanged.

Table 4. The values of AAE and SSA used for fresh and aged smoke conditions for BC and BrC.

| | BC | BrC |
|-----------------------|-------|-------|
| Fresh smoke dominated | | |
| AAE1 | 0.495 | 4.095 |
| AAE2 | 0.765 | 0 |
| SSA | 0.15 | 0.85 |
| Aged smoke dominated | | |
| AAE1 | 0.605 | 5.005 |
| AAE2 | 0.935 | 0 |
| SSA | 0.3 | 0.95 |

We chose Figure 5b,f, which were dominated by dust and carbonaceous aerosols, as examples for our study. Moreover, we still used the HSRL and sun photometer data corresponding to the scattered points in Figure 5. The different values of AAE and SSA in Table 4 were reused for the corresponding observational data, and a comparison curve (Figure 11) with Figure 5b,f (the original fitting curve) was obtained.

A comparison of Figure 11a,b, indicated that under the dust-dominated condition, the fitting curve obtained from fresh smoke with lower AAE and SSA values has smaller values than the original fitting curve. Moreover, the fitting curve obtained from aged smoke with larger AAE and SSA values had larger values than the original fitting curve because the dust fraction calculated by the lower AAE and SSA values was also smaller. A comparison of Figures 5b and 11a showed that the dust fraction of the scatter points in Figure 11a was concentrated in the range of 10–20%, which led to the fitting curve being smaller than the original fitting curve. For the aged smoke of carbonaceous aerosols, by comparing Figures 5b and 11b, it was found that the dust fraction of the scatter points in Figure 11b was concentrated in the range of 80–100%, which led to the fitting curve being larger than the original fitting curve. However, under the carbonaceous aerosol-dominated condition, since the lidar ratio increased with increasing aerosol fraction, Figure 11c,d yielded almost opposite conclusions to Figure 11a,b. Through the above comparison, we found that different types of aerosols affect the accuracy of the LR-AFNR, but at present, we have not further analyzed the influence of different types of aerosols on the LR-AFNR. We believe that a more refined classification of aerosol types is needed in the future to obtain a more credible LR-AFNR model, which is a worthy direction to work on.

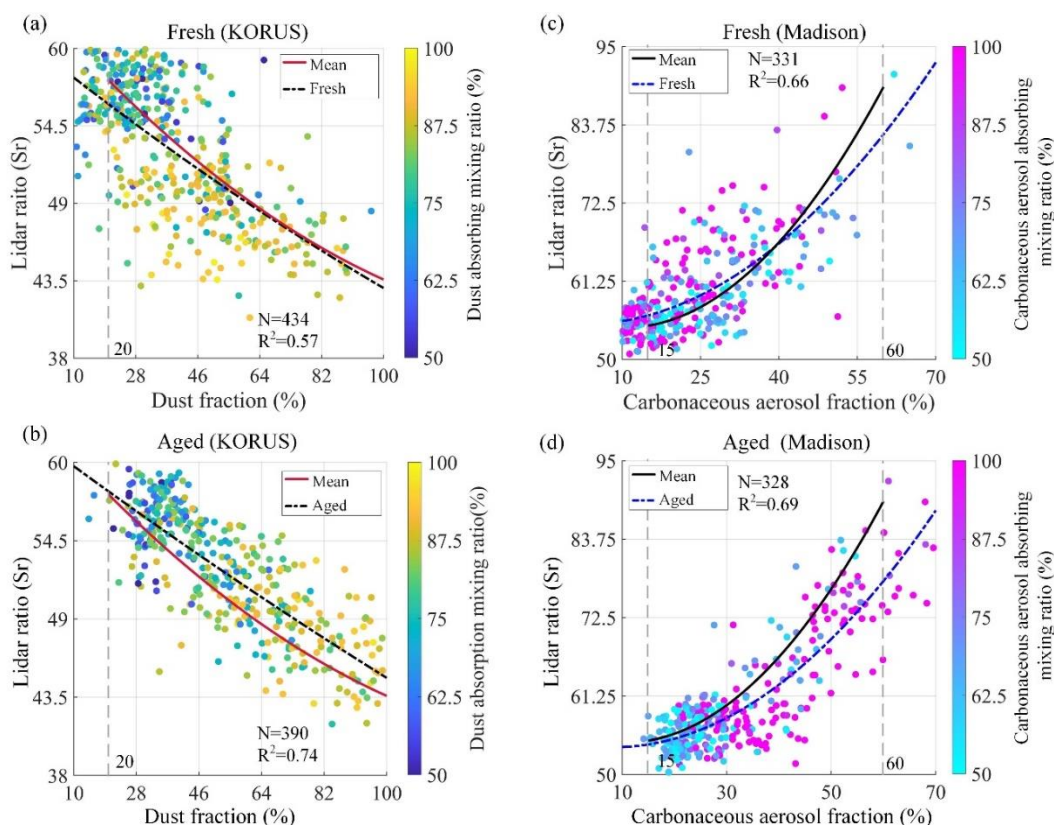


Figure 11. The influence of different types of carbonaceous aerosols (different AAEs and SSAs) on the fitting results of the LR-AFNR model. (a,b) represent the results of the fitting curves for different types of carbonaceous aerosols (fresh and aged) under dust-dominated conditions compared with the original fitting curve in Figure 5b. The solid red line represents the original fitting curve, and the black dotted lines represent the fitting curves of fresh and aged smoke; (c,d) represent the results of the fitting curves for different types of carbonaceous aerosols (fresh and aged) under carbonaceous aerosol-dominated conditions compared with the original fitting curve in Figure 5f. The solid black line represents the original fitting curve, and the blue dotted lines represent the fitting curves of fresh and aged smoke. N and R^2 represent the number of fitting points and the coefficient of determination, respectively. It should be noted that the solid red line corresponds to the dust fraction range of 20–100% in Figure 5b, and the solid black line corresponds to the carbonaceous aerosol fraction range of 15–60% in Figure 5f, so only part of the curve is shown in this Figure.

5. Conclusions

Based on the data of AERONET sites and University of Wisconsin HSRL sites in the same location, this paper developed a non-linear regression relationship between the absorbing aerosol (dust and carbonaceous aerosols) lidar ratio and corresponding fraction. The results show that the R^2 values were all higher than 0.5, which can be considered highly correlated. Then, the paper compared the fitting relationship of the two absorbing aerosols at each of the three sites and found similarities, and the LR-AFNR model was developed in this paper. A total of 63 AERONET sites in six regions were selected to study the model usage conditions. It was found that the model can control the relative error of α_a within 20% under the conditions of heavy dust and heavy carbonaceous aerosols when the usage range does not exceed 108 km and 85 km, and the maximum relative error of dust and carbonaceous α_a were reduced from 43% and 64% to 20%. According to the study results, this paper proposes a lidar network composed of HSRL and ML: put the HSRL in the center and deploy multiple MLs around it. All lidars are deployed in locations where sun photometers exist, such as in meteorological bureaus and universities. When the relative distance between the HSRL and the ML is within 85 km, the HSRL can be transferred to

the lidar ratio as the input parameters of the Klett–Fernald method retrieval for the ML through the sun photometer as the medium. In this way, this method implements the indirect transfer of the lidar ratio from HSRL to MLs.

However, this paper only discusses the model for dust and carbonaceous aerosols, and there is a lack of more in-depth research on the classification of refined aerosols. Through our research, we found that different types of aerosols would cause different AAE and SSA values, which would influence the accuracy of the LR-AFNR model. In addition, the accuracy of the LR-AFNR model was also affected by the different regions and other constraints. Therefore, it is necessary to promote the HSRL system in the future. More of the above-mentioned lidar networks should be deployed. Moreover, we should continuously improve the LR-AFNR model by using the lidar ratio obtained by HSRL and the relevant data obtained by sun photometers (or other relevant instruments) to develop the relationship between the relevant aerosol fraction and lidar ratio in different regions. This lidar network mode can also improve the detection accuracy of the internal MLs while controlling the cost. Combining the advantages of both lidars is of great significance for accurate monitoring research of the three-dimensional distribution of aerosols on a regional scale.

Author Contributions: The contribution of each author to this research article is specified as follows: Conceptualization, D.L.; Methodology Y.T., S.C. and D.L.; Validation, S.C. and D.L.; Data curation, D.X. and K.Z.; Writing—original draft preparation, Y.T. and S.C.; Writing—review and editing, Y.T., S.C., D.X., K.Z., J.F., C.L., Y.S. and D.L. All authors have read and agreed to the published version of the manuscript.

Funding: This research was funded by the National Key Research and Development Program of China (2016YFC0200700); the National Natural Science Foundation of China (NSFC) (41775023); the Excellent Young Scientist Program of the Zhejiang Provincial Natural Science Foundation of China (LR19D050001); the Public Welfare Project of Zhejiang Province (2016C33004); Fundamental Research Funds for the Central Universities (2019FZJD011); and the State Key Laboratory of Modern Optical Instrumentation Innovation Program.

Institutional Review Board Statement: Not applicable.

Informed Consent Statement: Not applicable.

Data Availability Statement: Not applicable.

Acknowledgments: The authors are grateful to the University of Wisconsin Lidar Group for making the HSRL data products publicly accessible. The lidar data used in work are available from <http://hsrl.ssec.wisc.edu> (5 January 2022). Moreover, we also are grateful to NASA's team for making the AERONET data products publicly accessible. The data used in work regarding aerosol fraction calculations are available from <https://aeronet.gsfc.nasa.gov> (5 January 2022).

Conflicts of Interest: The authors declare no conflict of interest.

Appendix A

This paper selected data from 63 sites in six regions for research. The location information can be found in Figure A1, and the specific site name, location, and data selection period time information can be found in Table A1.

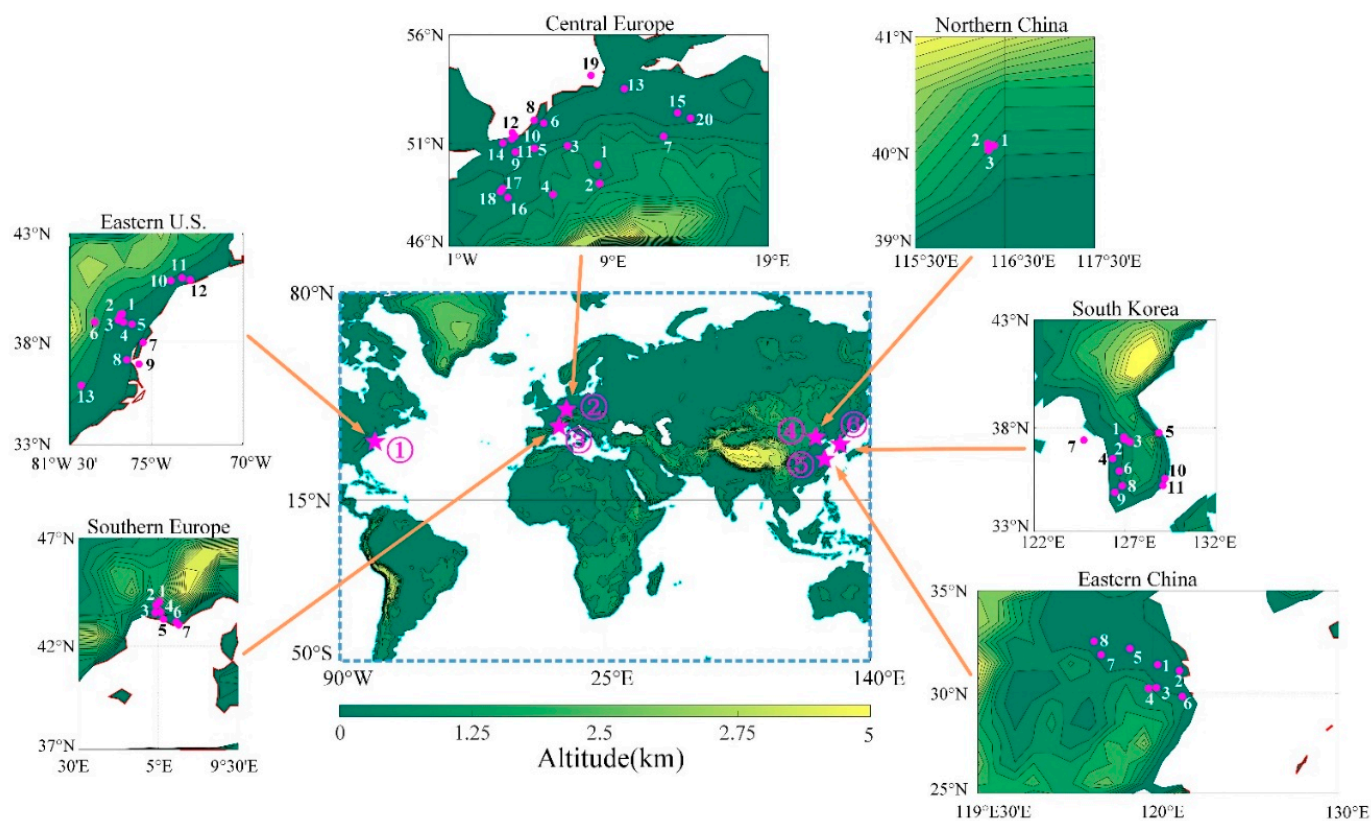


Figure A1. The six regional sites of AERONET are marked on the map. The regions ①–⑥ represent eastern U.S., northern Europe, northern Europe, northern China, eastern China, and South Korea, respectively. The six figures around the world map represent the detailed distribution map of the selected AERONET site locations in each region. The numbers in the figure correspond to the information of each corresponding numbered site in Table A1; where the color bar represents altitude, it should be noted that the figure omits six detailed figures of the color bar with an altitude range of 0~2 km.

Table A1. The information of the AERONET sites.

| | Number | Site Name | Latitude (°) | Longitude (°) | Altitude (m) | Selection Period |
|----------------|--------|---------------------|--------------|---------------|--------------|----------------------------|
| ① Eastern U.S. | 1 | MD Science Center | 39.28N | 76.61W | 15 | January 2001–March 2021 |
| | 2 | UMBC | 39.25N | 76.71W | 79 | July 2009–June 2016 |
| | 3 | GSFC | 38.99N | 76.84W | 87 | January 2001–March 2021 |
| | 4 | SERC | 38.89N | 76.56W | 36.5 | May 2001–March 2021 |
| | 5 | Easton-MDE | 38.80N | 76.08W | 4.5 | August 2014–September 2020 |
| | 6 | NEON_SCBI | 38.89N | 78.14W | 354 | December 2014–March 2021 |
| | 7 | Wallops | 37.93N | 75.47W | 13.5 | June 2001–January 2021 |
| | 8 | NASA LaRC | 37.11N | 76.38W | 5 | November 2004–March 2021 |
| | 9 | COVE | 36.90N | 75.71W | 24 | April 2005–January 2016 |
| | 10 | SEAPRISM | 36.90N | 75.71W | 24 | April 2005–January 2016 |
| | 11 | CCNY | 40.82N | 73.95W | 100 | December 2001–March 2021 |
| | 12 | LISCO | 40.95N | 73.34W | 12 | October 2009–March 2021 |
| | 13 | Brookhaven | 40.87N | 72.88W | 37 | September 2002–March 2021 |
| | | EPA-Res_Triangle_Pk | 35.88N | 78.87W | 109 | June 2013–March 2021 |

Table A1. Cont.

| | Number | Site Name | Latitude (°) | Longitude (°) | Altitude (m) | Selection Period |
|-------------------|--------|-------------------|--------------|---------------|--------------|------------------------------|
| ② Central Europe | 1 | Mainz | 50.00N | 8.30E | 150 | November 2003–March 2021 |
| | 2 | Karlsruhe | 49.09N | 8.43E | 140 | March 2005–March 2021 |
| | 3 | FZJ-JOYCE | 50.91N | 6.41E | 111 | July 2012–February 2021 |
| | 4 | Bure OPE | 48.56N | 5.51E | 393 | February 2021–March 2021 |
| | 5 | Brussels | 50.78N | 4.35E | 120 | July 2006–March 2021 |
| | 6 | Cabauw | 51.97N | 4.93E | -0.7 | February 2005–November 2020 |
| | 7 | Leipzig | 51.35N | 12.44E | 125 | May 2005–March 2021 |
| | 8 | The_Hague | 52.11N | 4.33E | 18 | February 2003–April 2006 |
| | 9 | Lille | 50.61N | 3.14E | 60 | May 2005–March 2021 |
| | 10 | Zeebrugge-MOW1 | 51.36N | 3.12E | 15 | February 2014–September 2019 |
| | 11 | Oostende | 51.23N | 2.93E | 23 | February 2005–June 2015 |
| | 12 | Thornton C-power | 51.53N | 2.96E | 30 | April 2015–November 2018 |
| | 13 | Hamburg | 53.57N | 9.97E | 120 | March 2005–September 2019 |
| | 14 | Dunkerque | 51.04N | 2.37E | 5 | May 2005–March 2021 |
| | 15 | Berlin FUB | 52.46N | 13.31E | 80 | July 2014–March 2021 |
| | 16 | Fontainebleau | 48.41N | 2.68E | 85 | February 2003–September 2008 |
| | 17 | Paris | 48.85N | 2.36E | 50 | January 2005–March 2021 |
| | 18 | Palaiseau | 48.71N | 2.22E | 156 | February 2005–March 2021 |
| | 19 | Helgoland MetObs | 54.18N | 7.89E | 33 | August 2005–June 2015 |
| | 20 | Lindenberg | 52.21N | 14.12E | 120 | September 2013–March 2021 |
| ③ Northern Europe | 1 | Carpentras | 44.08N | 5.06E | 107 | February 2003–November 2018 |
| | 2 | Avignon | 43.93N | 4.88E | 32 | December 2009–February 2013 |
| | 3 | Salon de Provence | 43.61N | 5.12E | 60 | January 2003–October 2012 |
| | 4 | La Crau | 43.58N | 4.82E | 32 | July 2010–January 2017 |
| | 5 | Frioul | 43.27N | 5.29E | 40 | June 2006–August 2019 |
| | 6 | Toulon | 43.14N | 6.01E | 50 | September 2003–March 2021 |
| | 7 | Porquerolles | 43.00N | 6.16E | 22 | May 2007–November 2014 |
| ④ Northern China | 1 | Beijing | 39.98N | 116.38E | 92 | January 2010–March 2021 |
| | 2 | Beijing RAD1 | 40.00N | 116.38E | 59 | January 2010–March 2021 |
| | 3 | Beijing PKU | 39.99N | 116.31E | 53 | June 2016–October 2019 |
| | 4 | Beijing CAMS | 39.93N | 116.32E | 106 | August 2012–March 2021 |
| ⑤ Eastern China | 1 | Taihu | 31.42N | 120.22E | 20 | September 2005–October 2018 |
| | 2 | Shanghi Minhang | 31.13N | 121.40E | 49 | March 2008–March 2010 |
| | 3 | Hangzhou City | 30.29N | 120.16E | 30 | April 2008–February 2012 |
| | 4 | Hangzhou-ZFU | 30.26N | 119.73E | 42 | August 2007–August 2009 |
| | 5 | NUIST | 32.21N | 118.72E | 62 | September 2007–December 2009 |
| | 6 | Ningbo | 29.86N | 121.55E | 37 | August 2007–September 2009 |
| | 7 | Hefei | 31.90N | 117.16E | 36 | December 2007–2009November |
| | 8 | Shouxian | 32.56N | 116.78E | 22.7 | May 2007–December 2009 |
| ⑥ South Korea | 1 | Yonsei University | 37.56N | 126.93E | 97 | February 2011–February 2021 |
| | 2 | Seoul SNU | 37.46N | 126.95E | 116 | February 2009–March 2021 |
| | 3 | Hankuk UFS | 37.34N | 127.27E | 167 | June 2012–March 2021 |
| | 4 | Anmyon | 36.54N | 126.33E | 47 | January 2014–March 2021 |
| | 5 | Gangneung WNU | 37.77N | 128.87E | 60 | June 2012–March 2021 |
| | 6 | DRAGON_Kunsan NU | 35.94N | 126.68E | 32 | March 2016–February 2017 |
| | 7 | Socheongcho | 37.42N | 124.74E | 28 | October 2015–March 2021 |
| | 8 | Gwangju GIST | 35.23N | 126.84E | 67 | April 2011–March 2021 |
| | 9 | KORUS Mokpo NU | 34.91N | 126.44E | 26 | March 2016–January 2017 |
| | 10 | KORUS UNIST Ulsan | 35.58N | 129.19E | 106 | March 2016–March 2021 |
| | 11 | Pusan NU | 35.24N | 129.08E | 78 | June 2012–February 2017 |

Table A2. The simulation parameter information of ZJU-HSRL.

| | Specification | Value |
|--------------------------|---|-------------------------|
| Transmitter | Laser energy E_0 (mJ) | 15 |
| | Laser wavelength λ (nm) | 532 |
| | Spot diameter ϕ_r (mm) | 2 |
| | Beam divergence θ_r (mrad) | 0.3 |
| | Optical axis spacing L (m) | 0.2 |
| Receiver | Focal length (mm) | 2800 |
| | Primary mirror diameter ϕ_1 (mm) | 280 |
| | Second mirror diameter ϕ_2 (mm) | 95 |
| | Field of view θ_t (mrad) | 0.5 |
| Photoelectric Detection | Filter bandwidth $\Delta\lambda$ (nm) | 1 |
| | Quantum efficiency η_Q (unit) | 0.15 |
| | Radiant (mA/W) | 75 |
| Wide bandwidth Amplifier | Gain (unit) | 5×10^4 |
| | Bandwidth (MHz) | 150 |
| | Conversion Factor (mV/mA) | 4000 |
| Data Acquisition | Sampling frequency Δt (MHz) | 20 |
| | Resolution (bit) | 16 |
| Other parameters | Planck's constant h (J·s) | 6.626×10^{-34} |
| | Speed of light c (m/s) | 3×10^8 |
| | solar spectral radiance reflected I_b ($\text{Wm}^{-2}\text{Sr}^{-1}\text{nm}^{-1}$) | 0.46×10^{-6} |

References

- Weitkamp, C. Introduction to lidar. In *Lidar, Range-Resolved Optical Remote Sensing of the Atmosphere*; Springer: Berlin/Heidelberg, Germany, 2005; Volume 102, pp. 1–18.
- Sugimoto, N.; Matsui, I.; Shimizu, A.; Nishizawa, T.; Hara, Y.; Uno, I. Lidar network observation of tropospheric aerosols. *Proc. SPIE-Int. Soc. Opt. Eng.* **2010**, *7860*, 78600J.
- Bösenberg, J.; Hoff, R.; Ansmann, A.; Müller, D.; Freudenthaler, V. Plan for the implementation of the GAW Aerosol Lidar Observation Network GALION. In Proceedings of the GAW Programme Reports, Hamburg, Germany, 27–29 March 2007.
- Pappalardo, G.; Amodeo, A.; Apituley, A.; Comeron, A.; Freudenthaler, V.; Linné, H.; Ansmann, A.; Bösenberg, J.; D'Amico, G.; Mattis, I.; et al. EARLINET: Towards an advanced sustainable European aerosol lidar network. *Atmos. Meas. Tech.* **2014**, *7*, 2929–2980. [[CrossRef](#)]
- Shimizu, A.; Nishizawa, T.; Jin, Y.; Kim, S.W.; Wang, Z.; Batdorj, D.; Sugimoto, N. Evolution of a lidar network for tropospheric aerosol detection in East Asia. *Opt. Eng.* **2016**, *56*, 031219. [[CrossRef](#)]
- Welton, E.J.; Campbell, J.R.; Berkoff, T.A.; Valencia, S.; Spinhirne, J.D.; Holben, B.; Tsay, S.C.; Schmid, B. The NASA Micro-Pulse Lidar Network (MPLNET): An overview and recent results. *Opt. Pura Apl.* **2006**, *39*, 67–72.
- Nishizawa, T.; Sugimoto, N.; Matsui, I.; Shimizu, A.; Higurashi, A.; Jin, Y. The Asian Dust and Aerosol Lidar Observation Network (AD-NET): Strategy and progress. *EPJ Web Conf.* **2016**, *119*, 19001. [[CrossRef](#)]
- Wang, N.; Shen, X.; Xiao, D.; Veselovskii, I.; Zhao, C.; Chen, F.; Liu, C.; Rong, Y.; Ke, J.; Wang, B.; et al. Development of ZJU high-spectral-resolution lidar for aerosol and cloud: Feature detection and classification. *J. Quant. Spectrosc. Radiat. Transf.* **2021**, *261*, 107513. [[CrossRef](#)]
- Böckmann, C.; Wandinger, U.; Ansmann, A.; Bösenberg, J.; Wiegner, M. Aerosol lidar intercomparison in the framework of the EARLINET project. 2. Aerosol backscatter algorithms. *Appl. Opt.* **2004**, *43*, 977–989. [[CrossRef](#)]
- Cheng, Z.; Liu, D.; Luo, J.; Yang, Y.; Su, L.; Yang, L.; Huang, H.; Shen, Y. Effects of spectral discrimination in high-spectral-resolution lidar on the retrieval errors for atmospheric aerosol optical properties. *Appl. Opt.* **2014**, *53*, 4386. [[CrossRef](#)]
- Fernald, F.G. Analysis of atmospheric lidar observations: Some comments. *Appl. Opt.* **1984**, *23*, 652. [[CrossRef](#)]
- Cheng, Z.; Liu, D.; Luo, J.; Yang, Y.; Zhou, Y.; Zhang, Y.; Duan, L.; Su, L.; Yang, L.; Shen, Y. Field-widened Michelson interferometer for spectral discrimination in high-spectral-resolution lidar: Theoretical framework. *Opt. Express* **2015**, *23*, 12117–12134. [[CrossRef](#)]

13. Siomos, N.; Balis, D.S.; Poupkou, A.; Liora, N.; Dimopoulos, S.; Melas, D.; Giannakaki, E.; Filioglou, M.; Basart, S.; Chaikovsky, A. Investigating the quality of modeled aerosol profiles based on combined lidar and sunphotometer data. *Atmos. Chem. Phys.* **2017**, *17*, 7003–7023. [[CrossRef](#)]
14. Groß, S.; Tesche, M.; Freudenthaler, V.; Toledano, C.; Wiegner, M.; Ansmann, A.; Althausen, D.; Seefeldner, M. Characterization of Saharan dust, marine aerosols and mixtures of biomass-burning aerosols and dust by means of multi-wavelength depolarization and Raman lidar measurements during SAMUM 2. *Tellus B* **2011**, *63*, 706–724. [[CrossRef](#)]
15. Bahadur, R.; Praveen, P.S.; Xu, Y.; Ramanathan, V. Solar absorption by elemental and brown carbon determined from spectral observations. *Proc. Natl. Acad. Sci. USA* **2012**, *109*, 17366–17371. [[CrossRef](#)] [[PubMed](#)]
16. Goloub, P.; Li, Z.; Dubovik, O.; Blarel, L.; Ramos, R. PHOTONS/AERONET sunphotometer network overview. Description—Activities—Results. *Proc. SPIE-Int. Soc. Opt. Eng.* **2008**, 6935, 69360V.
17. Lopes, F.J.S.; Landulfo, E.; Vaughan, M.A. Evaluating CALIPSO's 532 nm lidar ratio selection algorithm using AERONET sun photometers in Brazil. *Atmos. Meas. Tech.* **2013**, *6*, 3281–3299. [[CrossRef](#)]
18. Hoffer, A.; Gelencsér, A.; Guyon, P.; Kiss, G.; Schmid, O.; Frank, G.P.; Artaxo, P.; Andreae, M.O. Optical properties of humic-like substances (HULIS) in biomass-burning aerosols. *Atmos. Chem. Phys.* **2006**, *5*, 3563–3570. [[CrossRef](#)]
19. Liu, D.; Yang, Y.; Cheng, Z.; Huang, H.; Zhang, B.; Ling, T.; Shen, Y. Retrieval and analysis of a polarized high-spectral-resolution lidar for profiling aerosol optical properties. *Opt. Express* **2013**, *21*, 13084–13093. [[CrossRef](#)]
20. Xiao, D.; Wang, N.; Shen, X.; Landulfo, E.; Zhong, T.; Liu, D. Development of ZJU High-Spectral-Resolution Lidar for Aerosol and Cloud: Extinction Retrieval. *Remote Sens.* **2020**, *12*, 3047. [[CrossRef](#)]
21. Grund, C.J. University of Wisconsin High Spectral Resolution Lidar. *Opt. Eng.* **1991**, *30*, 6–12. [[CrossRef](#)]
22. Chen, S.; Russell, L.; Cappa, C.; Zhang, X.; Kleeman, M.; Kumar, A.; Liu, D.; Ramanathan, V. Comparing black and brown carbon absorption from AERONET and surface measurements at wintertime Fresno. *Atmos. Environ.* **2018**, *199*, 164–176. [[CrossRef](#)]
23. Chen, X.; Añel, J.; Su, Z.; Torre, L.; Kelder, H.; Peet, J.V.; Ma, Y. The deep atmospheric boundary layer and its significance to the stratosphere and troposphere exchange over the Tibetan Plateau. *PLoS ONE* **2013**, *8*, e56909. [[CrossRef](#)] [[PubMed](#)]
24. Messenger, C.; Parker, D.J.; Reitebuch, O.; Agusti-Panareda, A.; Taylor, C.M.; Cuesta, J. Structure and dynamics of the Saharan atmospheric boundary layer during the West African monsoon onset: Observations and analyses from the research flights of 14 and 17 July 2006. *Q. J. R. Meteorol. Soc.* **2010**, *136*, 107–124. [[CrossRef](#)]
25. Zhong, T.; Wang, N.; Shen, X.; Xiao, D.; Liu, D. Determination of planetary boundary layer height with lidar signals using maximum limited height initialization and range restriction (MLHI-RR). *Remote Sens.* **2020**, *12*, 2272. [[CrossRef](#)]
26. Tesche, M.; Müller, D.; Groß, S.; Ansmann, A.; Althausen, D.; Freudenthaler, V.; Weinzierl, B.; Lambert, A.; Petzold, A. Optical and microphysical properties of smoke over Cape Verde inferred from multiwavelength lidar measurements. *Tellus B* **2011**, *63*, 677–694. [[CrossRef](#)]
27. Tesche, M.; Ansmann, A.; Mueller, D.; Althausen, D.; Engelmann, R.; Hu, M.; Zhang, Y. Particle backscatter, extinction, and lidar ratio profiling with Raman lidar in south and north China. *Appl. Opt.* **2007**, *46*, 6302–6308. [[CrossRef](#)] [[PubMed](#)]
28. Wang, W.; Gong, W.; Mao, F.; Pan, Z.; Liu, B. Measurement and Study of Lidar Ratio by Using a Raman Lidar in Central China. *Int. J. Environ. Res. Public Health* **2016**, *13*, 508. [[CrossRef](#)] [[PubMed](#)]
29. Noh, Y.M.; Kim, Y.J.; Müller, D. Seasonal characteristics of lidar ratios measured with a Raman lidar at Gwangju, Korea in spring and autumn. *Atmos. Environ.* **2008**, *42*, 2208–2224. [[CrossRef](#)]
30. Jin, Y.; Krishnamurti, T.N.; Kim, J.; Kai, K.; Shibata, T.; Moriyama, T.; Zhang, K.; Zhou, H. Validation of the dust layer structure over the Taklimakan Desert, China by the CALIOP space-borne lidar using ground-based lidar. *Proc. SPIE-Int. Soc. Opt. Eng.* **2010**, *6*, 121–124. [[CrossRef](#)]
31. Burton, S.P.; Ferrare, R.A.; Hostetler, C.A.; Hair, J.W.; Rogers, R.R.; Obland, M.; Butler, C.F.; Cook, A.L.; Harper, D.B.; Froyd, K.D. Aerosol classification using airborne High Spectral Resolution Lidar measurements—Methodology and examples. *Atmos. Meas. Tech.* **2011**, *5*, 73–98. [[CrossRef](#)]
32. Sicard, M.; Mallet, M.; Vizcaíno, D.; Comeron, A.; Rocadenbosch, F.; Dubuisson, P.; Muñoz-Porcar, C. Intense dust and extremely fresh biomass burning outbreak in Barcelona, Spain: Characterization of their optical properties and estimation of their direct radiative forcing. *Environ. Res. Lett.* **2012**, *7*, 34016–34021. [[CrossRef](#)]
33. Chen, S.; Cheng, C.; Zhang, X.; Su, L.; Tong, B.; Dong, C.; Wang, F.; Chen, B.; Chen, W.; Liu, D. Construction of nighttime cloud layer height and classification of cloud types. *Remote Sens.* **2020**, *12*, 668. [[CrossRef](#)]
34. Hair, J.; Hostetler, C.; Cook, A.; Harper, D.; Ferrare, R.; Mack, T.; Welch, W.; Isquierdo, L.; Hovis, F. Airborne high spectral resolution lidar for profiling aerosol optical properties. *Appl. Opt.* **2009**, *47*, 6734–6752. [[CrossRef](#)] [[PubMed](#)]
35. Dubovik, O.; Smirnov, A.; Holben, B.N.; King, M.; Kaufman, Y.J.; Eck, T.F.; Slutsker, I. Accuracy assessments of aerosol optical properties retrieved from Aerosol Robotic Network (AERONET) Sun and sky radiance measurements. *J. Geophys. Res.* **2000**, *105*, 9791–9806. [[CrossRef](#)]
36. Holben, B.N.; Eck, T.F.; Slutsker, I.; Tanré, D.; Buis, J.P.; Setzer, A.; Vermote, E.; Reagan, J.A.; Kaufman, Y.J.; Nakajima, T. AERONET—A Federated Instrument Network and Data Archive for Aerosol Characterization. *Remote Sens. Environ.* **1998**, *66*, 1–16. [[CrossRef](#)]
37. Tan, S.C.; Li, J.; Che, H.; Chen, B.; Wang, H. Transport of East Asian dust storms to the marginal seas of China and the southern North Pacific in spring 2010. *Atmos. Environ.* **2016**, *148*, 316–328. [[CrossRef](#)]

38. Theodoritsi, G.N.; Posner, L.N.; Robinson, A.L.; Yarwood, G.; Pandis, S.N. Biomass burning organic aerosol from prescribed burning and other activities in the United States. *Atmos. Environ.* **2020**, *241*, 117753. [[CrossRef](#)]
39. Taylor, R. Interpretation of the Correlation Coefficient: A Basic Review. *J. Diagn. Med. Sonogr.* **1990**, *6*, 35–39. [[CrossRef](#)]
40. Veselovskii, I.; Kolgotin, A.; Griaznov, V.; Müller, D.; Wandinger, U.; Whiteman, D.N. Inversion with regularization for the retrieval of tropospheric aerosol parameters from multiwavelength lidar sounding. *Appl. Opt.* **2002**, *41*, 3685–3699. [[CrossRef](#)]
41. Liu, Z.; Voelger, P.; Sugimoto, N. Simulations of the observation of clouds and aerosols with the Experimental Lidar in Space Equipment system. *Appl. Opt.* **2000**, *39*, 3120–3137. [[CrossRef](#)]
42. Shen, X.; Wang, N.; Veselovskii, I.; Xiao, D.; Liu, D. Development of ZJU high-spectral-resolution lidar for aerosol and cloud: Calibration of overlap function. *J. Quant. Spectrosc. Radiat. Transfer* **2021**, *257*, 107338. [[CrossRef](#)]
43. Wu, Y.; Graaf, M.; Menenti, M. The sensitivity of AOD retrieval to aerosol type and vertical distribution over land with MODIS data. *Remote Sens.* **2016**, *8*, 765. [[CrossRef](#)]
44. Qiao, Z.; Wan, Z.; Xie, G.; Wang, J.; Qian, L.; Fan, D. Multi-vortex laser enabling spatial and temporal encoding. *Photonix* **2020**, *1*, 13. [[CrossRef](#)]
45. Gu, C.; Zuo, Z.; Luo, D.; Deng, Z.; Liu, Y.; Hu, M.; Li, W. Passive coherent dual-comb spectroscopy based on optical-optical modulation with free running lasers. *Photonix* **2020**, *1*, 7. [[CrossRef](#)]
46. Ji, H.; Chen, S.; Zhang, Y.; Chen, H.; Guo, P.; Chen, H. Calibration method for the reference parameter in Fernald and Klett inversion combining Raman and Elastic return. *J. Quant. Spectrosc. Radiat. Transfer* **2016**, *188*. [[CrossRef](#)]
47. Liu, Z.; Hunt, W.; Vaughan, M.; Hostetler, C.; Hu, Y. Estimating random errors due to shot noise in backscatter lidar observations. *Appl. Opt.* **2006**, *45*, 4437–4447. [[CrossRef](#)] [[PubMed](#)]
48. Stihler, C.; Jauregui, C.; Kholaf, S.E.; Limpert, J. Intensity noise as a driver for transverse mode instability in fiber amplifiers. *Photonix* **2020**, *1*, 8. [[CrossRef](#)]
49. Bian, Q.; Ford, B.; Pierce, J.R.; Kreidenweis, S.M. A decadal climatology of chemical, physical, and optical properties of ambient smoke in the western and southeastern U.S. *J. Geophys. Res. Atmos.* **2019**, *125*, e2019JD031372.
50. Russell, P.B.; Bergstrom, R.W.; Shinzuka, Y.; Clarke, A.D.; Decarlo, P.F.; Jimenez, J.L.; Livingston, J.M.; Redemann, J.; Dubovik, O.; Strawa, A. Absorption Angstrom Exponent in AERONET and related data as an indicator of aerosol composition. *Atmos. Chem. Phys.* **2010**, *10*, 1155–1169. [[CrossRef](#)]
51. Reid, J.S.; Eck, T.F.; Christopher, S.A.; Koppmann, R.; Zhang, J. A review of biomass burning emissions part III: Intensive optical properties of biomass burning particles. *Atmos. Chem. Phys.* **2004**, *5*, 827–849. [[CrossRef](#)]